

Pressure-induced metallization and Lifshitz transition in quasi-one-dimensional $TiSe_3$ single crystal

Zhenhai Yu(于振海), Yunguan Ye(叶运观), Pengtao Yang(杨芃焘), Yiming Wang(王弈铭), Liucheng Chen(陈刘城), Chenglin Li(李承霖), Jian Yuan(袁健), Ziyi Liu(刘子儀), Zhiwei Shen(申志伟), Shaojie Wang(王邵杰), Mingtao Li(李明涛), Chaoyang Chu(楚朝阳), Xia Wang(王霞), Jun Li(李俊), Lin Wang(王霖), Wenge Yang(杨文革), and Yanfeng Guo(郭艳峰)

Citation: Chin. Phys. B, 2025, 34 (**8**): 088102. DOI: 10.1088/1674-1056/adce9d
http://cpb.iphy.ac.cn; http://iopscience.iop.org/cpb

What follows is a list of articles you may be interested in

Single crystal growth and characterization of 166-type magnetic kagome metals

Huangyu Wu(吴黄宇), Jinjin Liu(刘锦锦), Yongkai Li(李永恺), Peng Zhu(朱鹏), Liu Yang(杨柳), Fuhong Chen(陈富红), Deng Hu(胡灯), and Zhiwei Wang(王秩伟)

Chin. Phys. B, 2024, 33 (**9**): 098101. DOI: 10.1088/1674-1056/ad553b

Single crystal growth and transport properties of narrow-bandgap semiconductor RhP_2

De-Sheng Wu(吴德胜), Ping Zheng(郑萍), and Jian-Lin Luo(雒建林)

Chin. Phys. B, 2024, 33 (**8**): 088101. DOI: 10.1088/1674-1056/ad4cd5

A new transition metal diphosphide α-MoP_2 synthesized by a high-temperature and high-pressure technique

Xiaolei Liu(刘晓磊), Zhenhai Yu(于振海), Jianfu Li(李建福), Zhenzhen Xu(徐真真), Chunyin Zhou(周春银), Zhaohui Dong(董朝辉), Lili Zhang(张丽丽), Xia Wang(王霞), Na Yu(余娜), Zhiqiang Zou(邹志强),Xiaoli Wang(王晓丽), and Yanfeng Guo(郭艳峰)

Chin. Phys. B, 2023, 32 (**1**): 018102. DOI: 10.1088/1674-1056/ac633d

Spin glassy behavior and large exchange bias effect in cubic perovskite $Ba_{0.8}Sr_{0.2}FeO_{3-\delta}$

Yu-Xuan Liu(刘宇轩), Zhe-Hong Liu(刘哲宏), Xu-Bin Ye(叶旭斌), Xu-Dong Shen(申旭东), Xiao Wang(王潇), Bo-Wen Zhou(周博文), Guang-Hui Zhou(周光辉), You-Wen Long(龙有文)

Chin. Phys. B, 2019, 28 (**6**): 068104. DOI: 10.1088/1674-1056/28/6/068104

A-site ordered quadruple perovskite oxides $AA_3'B_4O_{12}$

Youwen Long(龙有文)

Chin. Phys. B, 2016, 25 (**7**): 078108. DOI: 10.1088/1674-1056/25/7/078108

SPECIAL TOPIC — Structures and properties of materials under high pressure

Pressure-induced metallization and Lifshitz transition in quasi-one-dimensional $TiSe_3$ single crystal

Zhenhai Yu(于振海)[1,†], Yunguan Ye(叶运观)[1,†], Pengtao Yang(杨芃焘)[2,†], Yiming Wang(王弈铭)[3,†], Liucheng Chen(陈刘城)[2], Chenglin Li(李承霖)[2], Jian Yuan(袁健)[1], Ziyi Liu(刘子儀)[2], Zhiwei Shen(申志伟)[4], Shaojie Wang(王邵杰)[4], Mingtao Li(李明涛)[3], Chaoyang Chu(楚朝阳)[1], Xia Wang(王霞)[5], Jun Li(李俊)[2], Lin Wang(王霖)[4,‡], Wenge Yang(杨文革)[3,§], and Yanfeng Guo(郭艳峰)[1,6,¶]

[1] *School of Physical Science and Technology, ShanghaiTech University, Shanghai* 201210, *China*
[2] *Institute of Physics and Beijing National Laboratory for Condensed Matter Physics, Chinese Academy of Sciences, Beijing* 100190, *China*
[3] *Center for High Pressure Science and Technology Advanced Research, Shanghai* 201203, *China*
[4] *Center for High Pressure Science (CHiPS), State Key Laboratory of Metastable Materials Science and Technology, Yanshan University, Qinhuangdao* 066004, *China*
[5] *Analytical Instrumentation Center, School of Physical Science and Technology, ShanghaiTech University, Shanghai* 201210, *China*
[6] *ShanghaiTech Laboratory for Topological Physics, ShanghaiTech University, Shanghai* 201210, *China*

(Received 26 February 2025; revised manuscript received 1 April 2025; accepted manuscript online 21 April 2025)

The transition metal trichalcogenides (TMTs) with quasi-one-dimensional (quasi-1D) layered crystal structure represent a unique platform to explore intriguing physical properties. Herein, we report the successful growth of a new TMT $TiSe_3$ single crystal by using a high-pressure and high-temperature technique. The crystal structure of $TiSe_3$ was determined by measuring the single-crystal x-ray diffraction and selected area electron diffraction. The 1D chain-like structure along the *b*-axis is formed by the $TiSe_6$ prisms which share their tops and bottoms with each other. $TiSe_3$ is a narrow band gap semiconductor with electron-type carriers under ambient conditions identified by the electrical and Hall effect measurements. It exhibits a pressure-induced semiconductor-to-metal transition around 4 GPa. As the pressure further increases to $\sim$ 6 GPa, a pressure-induced Lifshitz transition occurs, as indicated by the electrical transport measurements, high-pressure crystal structure characterizations, and electronic band structure calculations.

Keywords: high-pressure synthesis, transition metal trichalcogenides, quasi-one-dimensional layered crystal structure, Lifshitz transition

PACS: 81.10.–h, 61.50.Ah, 68.65.–k, 61.50.Ks

DOI: 10.1088/1674-1056/adce9d **CSTR:** 32038.14.CPB.adce9d

1. Introduction

The successful exfoliation of graphene[1] opened a new window for the study of various layered structured materials. The layered transition metal dichalcogenides have captured special interest because they are conceived as promising materials for next-generation electronic and optoelectronic devices,[2,3] due to their combination of exfoliated atomic-scale thickness and other exotic physical properties.[4,5] Among them, the transition metal trichalcogenides (TMTs) MX_3, where M is a transition metal atom (group IV, V, or VI) and X is a chalcogen atom (such as S, Se, or Te), represent an excellent platform to explore intriguing physical properties. The structure of TMTs is formed by linking the strong covalent bonds in the one-dimensional (1D) chain direction, with weaker covalent bonds between adjacent chains. These bonds arrange the 1D chains into 2D sheets, providing TMTs with the virtues of both 1D and two-dimensional (2D) features.[6,7] Among the nine group IVB TMTs materials including TiS_3, $TiSe_3$, $TiTe_3$, ZrS_3, $ZrSe_3$, $ZrTe_3$, HfS_3, $HfSe_3$, and $HfTe_3$, all except for the $TiSe_3$ and $TiTe_3$ have already been reported. Regarding the rich and intriguing properties of this family of materials, it would be very valuable to synthesize both $TiSe_3$ and $TiTe_3$.

The Ti–Se binary phase diagram at ambient pressure was already investigated, which includes Ti_9Se_2, $Ti_{45}Se_{16}$, Ti_8Se_3, Ti_2Se, Ti_5Se_4, TiSe, Ti_3Se_4, Ti_2Se_3, $TiSe_2$, etc.[8,9] Apparently, the most Se-rich Ti–Se binary compound in this family is $TiSe_2$. First-principles calculations on the cohesive and formation energies of MX_3 (M = Ti, Zr, and Hf, X = S, Se, and Te) indicated that they both have negative values, suggesting that $TiSe_3$ and $TiTe_3$ could be experimentally synthesized by adopting appropriate synthesis techniques.[10] Besides, a theoretical study on the pressure–composition phase diagram of

[†]These authors contributed equally to this work.
[‡]Corresponding author. E-mail: linwang@ysu.edu.cn
[§]Corresponding author. E-mail: yangwg@hpstar.ac.cn
[¶]Corresponding author. E-mail: guoyf@shanghaitech.edu.cn

© 2025 Chinese Physical Society and IOP Publishing Ltd. All rights, including for text and data mining, AI training, and similar technologies, are reserved.

the Ti–Se system revealed that $TiSe_3$ could be stable under high pressure between 15–30 GPa.[11–13]

We herein report for the first time the successful growth of a $TiSe_3$ single crystal using the high-pressure and high-temperature (HPHT) technique. We also investigated the crystal structure and electrical transport properties of $TiSe_3$ under high pressure up to 14.5 GPa.

2. Experimental and computational details

Starting materials Ti and Se powders were mixed in a molar ratio of Ti:Se = 1:3 in an Ar-filled glove box. The mixture was pre-compressed into a cylinder, and then put into a hexagonal boron nitride chamber. This sample chamber was placed into a Ta heating furnace and then was packed in an MgO octahedron. The assembly was pressed in a multi-anvil apparatus at 6–8 GPa and 800–1000 °C for 30 minutes. Detailed information about the HPHT synthesis can be found in our previous work.[14]

The stoichiometry of $TiSe_3$ was checked by measuring energy dispersive spectroscopy (EDS) on many arbitrarily selected microcrystals cracked from a bulk crystal. The crystallographic phase and crystal quality examinations of $TiSe_3$ single crystals were examined using a Bruker D8 single-crystal x-ray diffractometer (SXRD) with Mo $K\alpha$ ($\lambda = 0.71073$ Å) at 150.0 K. The structure was solved using Olex2[15] with the SHELXT[16] structure solution program and refined with the SHELXL[17] refinement package using least-square minimization. Selected area electron diffraction (SAED) measurements on $TiSe_3$ single crystals were carried out using an ultrafast transmission electron microscope at the Synergic Extreme Condition User Facility (SECUF) at Huairou. The Raman spectrum of $TiSe_3$ was measured using a commercial Raman spectroscopy system in the backscattering configuration excited with a He/Ne laser ($\lambda = 532$ nm). The electrical transport measurements including electrical and Hall resistivity (ρ_{xx} and ρ_{xy}) under ambient pressure were performed in a Quantum Design physical property measurement system. The electrical resistivity was measured in a standard four-probe configuration by attaching Au wires with silver paste to the sample. The Hall effect measurements were carried out using a standard Hall bar geometry.

To examine whether pressure-induced structural phase transitions occur in $TiSe_3$, we performed high-pressure x-ray diffraction (HP-XRD) measurements. The measurement on $TiSe_3$ was carried out using a symmetric-type diamond anvil cell (DAC) with a diamond culet size of 500 μm. Silicone oil was used as the pressure transmitting medium (PTM). The pressure in the DAC was measured using the ruby fluorescence technique.[18] HP-XRD patterns were collected using laboratory x-ray diffractometer with a wavelength of 0.5594 Å. The XRD patterns of $TiSe_3$ were analyzed with Rietveld refinement using the GSAS program package[19] with the user interface EXPGUI.[20]

The high-pressure and low-temperature electrical transport experiments using a cubic anvil cell (CAC) were performed at the SECUF. Electrical resistivity under high pressure was measured using the standard four-probe method. Glycerol was employed as the PTM for resistivity measurements. Pressure values in the CAC chamber were estimated from the calibration curve determined by the shift in the superconducting transition temperature of Pb at low temperatures.[21] The maximum pressure and lowest temperature achieved during the measurement were 13 GPa and 1.6 K, respectively.

All calculations were conducted within the framework of density functional theory (DFT)[22,23] using the projector augmented wave[24,25] pseudopotential method, as implemented in the VASP package.[26,27] The electron exchange–correlation functional was treated using generalized gradient approximation as proposed by Perdew–Burke–Ernzerhof (PBE). Grimme's DFT-D3 dispersion correction[28] was applied to account for the long-range van der Waals interactions. The valence electrons were considered as $3s^2 3p^6 3d^3 4s^1$ for Ti and $4s^2 4p^4$ for Se. The kinetic energy cutoff for the plane-wave basis set expansion was set to 420 eV in all cases to avoid Pulay stress. The Brillouin zone was sampled by a Γ-centered Monkhorst–Pack mesh with 0.2 $Å^{-1}$ as the spacing between k-points. The energy convergence of 1.0×10^{-6} eV was used for the electronic energy minimization steps, and the force acting on each atom was set to be less than 0.01 eV/Å.

Since the PBE functional tends to underestimate the band gap, the Heyd–Scuseria–Ernzerhof (HSE) calculations with the hybrid functional, HSE06,[29] were adopted to obtain an accurate band structure of $TiSe_3$. The spatial decay of the Hartree–Fock (HF) exchange interaction is accelerated by the substitution of the bare full $1/r$ Coulomb potential with a screened one. The exchange–correlation energy is then calculated as follows:

$$E_{\mathrm{xc}}^{\mathrm{HSE}} = aE_{\mathrm{x}}^{\mathrm{HF,SR}}(\omega) + (1-a)E_{\mathrm{x}}^{\mathrm{PBE,SR}}(\omega) + E_{\mathrm{x}}^{\mathrm{PBE,LR}}(\omega) + E_{\mathrm{c}}^{\mathrm{PBE}},$$

where $\omega = 0.20$ $Å^{-1}$ is a parameter that specifies the range-separation between the short-range (SR) and long-range (LR) parts of the Coulomb kernel, while the adjustable parameter a (0.45 in this work) controls the fraction of the exact HF exchange to be incorporated.

3. Results and discussion

Figure 1(a) shows an optical picture of typical $TiSe_3$ single crystals. The morphology of the $TiSe_3$ single crystal shows a filamentous shape with a length of 1–2 mm, because crystal growth is along the b-axis with a 1D chain. An enlarged view

of the $TiSe_3$ single crystal surface is shown in Fig. 1(b). The SAED image in Fig. 1(c), viewed along the [001] zone, displays the reciprocal lattice of $TiSe_3$ at 300 K. The high crystal quality was demonstrated by the clear and bright diffraction spots without any other miscellaneous points. The EDS results confirm that the average compositions measured at different points on the crystal show good stoichiometry, with an atomic ratio of Ti:Se (25.49%:74.51%) = 1:3, as shown in Fig. 1(d).

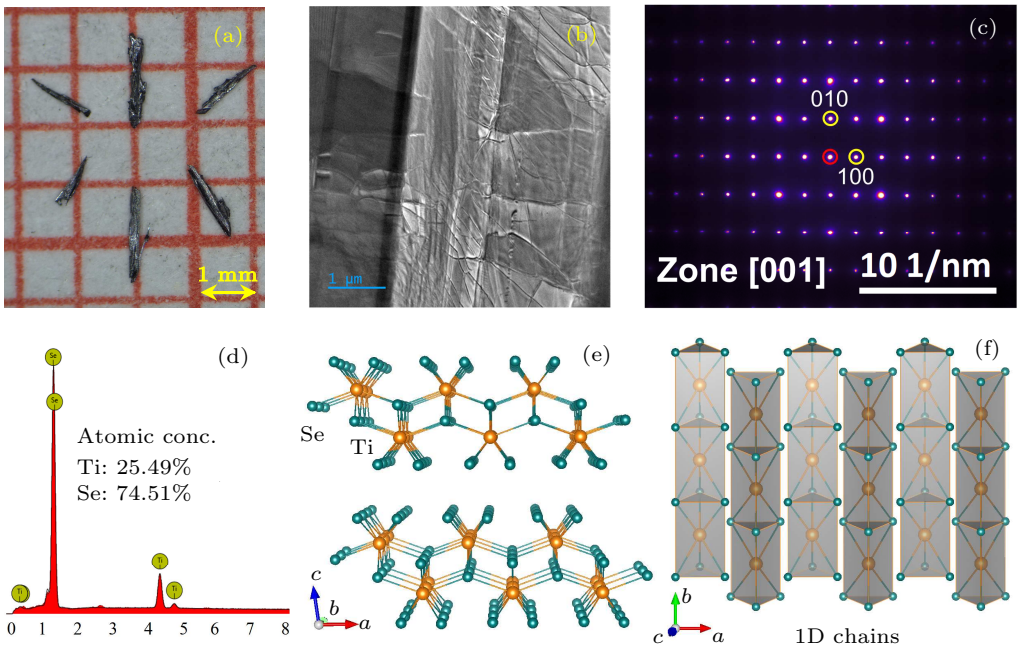


Fig. 1. (a) Optical picture of $TiSe_3$ single crystals. (b) The enlarged morphology taken by TEM. (c) Experimental SAED image obtained from the [001] zone axis at 300 K. (d) The measured average stoichiometric ratio is Ti:Se=1:3. (e) The $TiSe_8$ polyhedra were stacked to form 2D layers along the *a*-axis, while these layers were bonded by weak vdW force along the *c*-axis. (f) The $TiSe_6$ trigonal prisms connected face-to-face show the typical 1D chains along the *b*-axis, which result in its filamentous morphology.

The crystallographic information file (CIF) of $TiSe_3$ was obtained through refining the SXRD data. The parameters for data collection and refinement results are summarized in Table 1. Atomic coordinates and thermal displacement parameters (U_{eq}) are provided in Table 2. $TiSe_3$ crystallizes into a low-symmetry monoclinic $ZrSe_3$-type structure with space group $P2_1/m$. Unlike the prototypical charge-density-wave (CDW) materials TaS_3 and $NbSe_3$ which crystallize with two and three inequivalent chains per unit cell, respectively, $TiSe_3$ has only one type of chain per unit cell. The $TiSe_8$ polyhedron, with varying bond lengths, forms a layer that tessellates the *ab*-planes. The planes are connected by weak van der Waals (vdW) forces along the *c*-axis, as shown in Fig. 1(e). The crystal structure of $TiSe_3$ is comprised of trigonal prisms formed from Se_2^{-2} and Se^{2-} anions flanking a Ti^{4+} cation,[30] which stack along the *b*-axis and thus form a 1D chain-like structure, as shown in Fig. 1(f).

The experimental lattice parameters of $TiSe_3$ can then be compared with those theoretically calculated.[31] The theoretically optimized structural lattice parameters for $TiSe_3$ are $a = 5.328$ Å, $b = 3.538$ Å, and $\beta = 97.56°$, while c was not reported. In two other theoretical studies, the simulated lattice parameters of $TiSe_3$ are $a = 5.42$ Å, $b = 3.58$ Å, $c = 9.49$ Å, $\beta = 97.94°$,[10] and $a = 5.24$ Å, $b = 3.53$ Å, $c = 9.40$ Å, $\beta = 96.69°$,[32] respectively. They are all apparently close agreement with the present experimental results which are with $a = 5.269(3)$ Å, $b = 3.5353(17)$ Å, $c = 9.235(6)$ Å, and $\beta = 98.10(2)°$.

Table 1. Crystal information and structure refinement results for $TiSe_3$ at 150.0 K.

Empirical formula	$TiSe_3$
Formula weight	284.78
Temperature	150.0 K
Crystal system	monoclinic
Space group	$P2_1/m$
Unit cell dimens	$a = 5.269(3)$ Å, $\alpha = 90°$ $b = 3.5353(17)$ Å, $\beta = 98.10(2)°$ $c = 9.235(6)$ Å, $\gamma = 90°$
Volume	170.29(16) Å^3
Formula units per unit cell Z	2
Density (calcd)	5.554 g/cm^3
Absorption coefficient	34.282 mm^{-1}
Zeroth-order structure factor F (000)	248.0
Crystal size (mm^3)	$0.1 \times 0.15 \times 0.4$
Radiation	Mo $K\alpha$ ($\lambda = 0.71073$ Å)
2θ range for data collection	4.456° to 52.668°
Index ranges	$-6 \le h \le 6$, $-4 \le k \le 4$, $-11 \le l \le 11$
Reflections collected	2655
Independent reflections	402 [$R_{int} = 0.1239$, $R_{sigma} = 0.3274$]
Data/restraints/parameters	402/0/25
Goodness of fit on F^2	1.287
Final R indexes [$I \ge 2\sigma(I)$]	$R_1 = 0.1239$, $wR_2 = 0.3274$
Final R indexes (all data)	$R_1 = 0.1369$, $wR_2 = 0.3212$
Largest diff. peak/hole/e (Å^{-3})	6.330/–6.270

Table 2. Atomic coordinates and equivalent isotropic displacement parameters for $TiSe_3$.

	Wyckoff	x	y	z	U_{eq}
Ti	2*e*	0.7137	0.75	0.3432	0.027
Se(1)	2*e*	0.7597	0.25	0.5502	0.026
Se(2)	2*e*	0.4520	0.25	0.1769	0.028
Se(3)	2*e*	0.8859	0.25	0.1705	0.030

The three typical structural prototypes for TMTs are $ZrSe_3$-type ($P2_1/m$, $Z=2$), $NbSe_3$-type ($P2_1/m$, $Z=6$), and $TaSe_3$-type ($P2_1/m$, $Z=4$), as shown in Figs. 2(a)–2(c). The diversity of elements and differences in the shape and assembly mode of the 1D chains in TMTs lead to their varied electrical transport properties which cover insulators, semiconductors, and metals. Figure 2(d) shows the temperature dependence of a resistivity of $TiSe_3$ single crystal along the *b*-axis under ambient pressure. The resistivity increases with decreasing temperature, showing a variation of about four orders of magnitude between 50 K and 300 K and manifesting semiconducting conduction behavior. The inset of Fig. 2(d) shows the $\ln\rho(T)$ versus $1000/T$ data fitted with the thermal activation model $\rho(T)=\rho_0\exp(E_\alpha/(k_BT))$, where ρ_0 is a pre-exponential factor, E_α is the activation energy, and k_B is the Boltzmann constant. The red solid line denotes the linear fit of $\ln\rho(T)$ versus $1000/T$ in the temperature range of 55 K to 110 K. The fitting yields an activation energy $E_\alpha=58.6$ meV. Thus, the band gap of $TiSe_3$ is estimated to be ~ 117 meV, which is roughly consistent with the simulated values.[30,31]

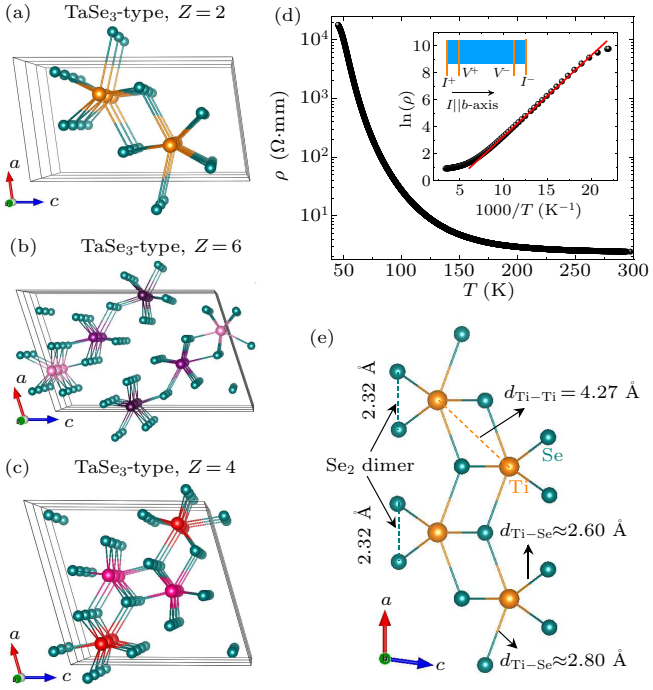


Fig. 2. (a)–(c) The three typical structural prototypes ($ZrSe_3$-type, $Z=2$, $NbSe_3$-type, $Z=6$, and $TaSe_3$-type, $Z=4$) for TMTs. (d) Temperature dependence of resistivity for $TiSe_3$ along the *b*-axis under ambient pressure. The insets show the resistivity data fitting with the thermal activation model and the schematic measurement configuration. (e) Projection along (010) of the $TiSe_3$ lattice as well as selected atomic distances.

The electrical transport property of $TiSe_3$ is closely related to its quasi-1D crystal structure. In $TiSe_3$, the Ti ion is located at the center of a slanted trigonal prism, with stacked trigonal faces forming separate columns along the *b*-axis, as shown in Fig. 1(f). Each Ti atom has two Se neighbors in adjacent $TiSe_6$ prisms at distances ($d_{Ti-Se}\cong 2.80$ Å) longer than those of its six intra-prism ligands ($d_{Ti-Se}\cong 2.60$ Å) as shown in Fig. 2(e). In addition, the Se-Se distance is determined to be $d_{Se-Se}\cong 2.32$ Å, which corresponds to the formation of $(Se_2)^{2-}$ dimer, as shown in Fig. 2(e). The Se dimers in one layer are oriented perpendicular to those in neighboring layers.[33] These crystalline characteristics result in the formation of $(Se^{2-})(Se_2^{2-})$ and the Ti oxidation state being Ti^{4+} (d^0), leading to empty *d*-block bands of Ti.[30] Due to this electronic configuration, most TMTs, including the present synthesized $TiSe_3$, are semiconductors.[34]

To investigate the carrier type in $TiSe_3$, the Hall effect of $TiSe_3$ was measured under ambient pressure. The slope of ρ_{xy} versus magnetic field is negative, as seen from Figs. 3(a)–3(c), indicating that electrons are the dominant carriers in $TiSe_3$. The magnetic field-dependent Hall resistivity shows linear behavior, suggesting that one type of carrier dominates the electrical conduction. Figure 3(d) shows the temperature dependence of the carrier density. It is remarkable to note that the carrier density shows an abrupt increase of about four orders of magnitude from 50 K to 300 K.

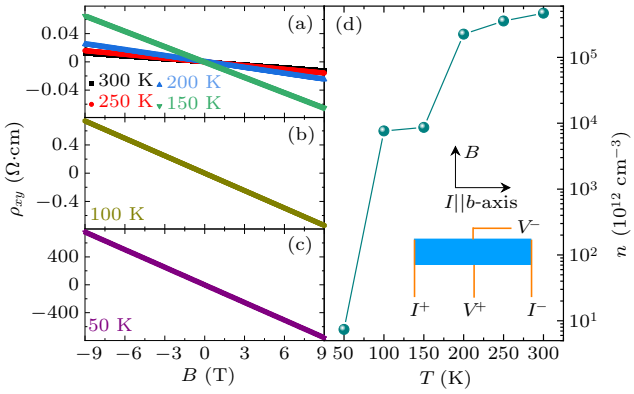


Fig. 3. (a)–(c) The Hall resistivity ρ_{xy} of $TiSe_3$ at selected temperatures under ambient pressure. (d) Carrier density as a function of temperature. The inset shows the schematic measurement configuration.

$TiSe_3$ belongs to the C_{2h} ($2/m$) point group with two formula units per unit cell. The 24 normal modes at the center Γ of the Brillouin zone are represented by the irreducible representations of the C_{2h} point group: $8A_g+4B_g+4A_u+8B_u$, of which 12 even-parity modes are Raman active ($8A_g+4B_g$), and the other 9 odd-parity modes ($2A_u+7B_u$) are infrared active, as shown in Fig. 4(a). The lower panel of Fig. 4(a) shows the Raman tensors and displacement directions of A_g and B_g modes. Atomic displacements associated with A_g and B_g Raman modes are perpendicular and parallel to the *b*-axis, respectively. The typical Raman spectrum of $TiSe_3$ under am-

bient conditions is shown in Fig. 4(b). Among the 12 Raman-active modes, the A_g^3, Ag^5, Ag^6, and Ag^8 modes appear near 113 cm^{-1}, 181 cm^{-1}, 271 cm^{-1} and 330 cm^{-1}, respectively. The Raman peak positions of isostructural TMTs including TiS_3, ZrS_3 and $ZrSe_3$,[35,36] are also marked in Fig. 4(b) with short vertical lines for easy comparison. In this study, only several A_g Raman modes were detected, and the intensity of B_g mode is very weak and almost indistinguishable. This phenomenon is also found in other TMTs, where the intensity of the B_g mode is much weaker than that of the A_g mode.[35]

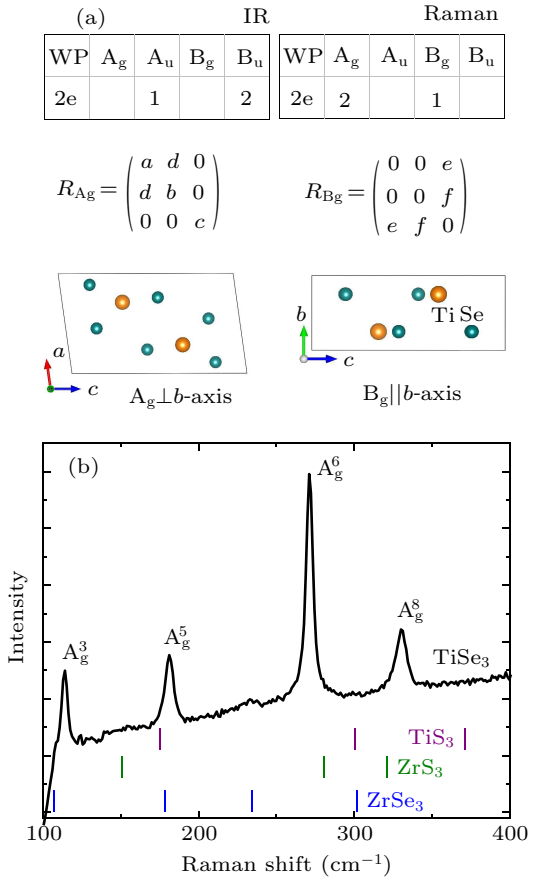


Fig. 4. (a) IR and Raman active modes of $TiSe_3$ with the C_{2h} $(2/m)$ point group, where WP denotes the Wyckoff position. The Raman tensors and displacement directions for the A_g and B_g modes are also presented. (b) Raman spectrum of $TiSe_3$ measured under ambient conditions. The Raman scattering peaks of TiS_3, ZrS_3 and $ZrSe_3$ are from literature,[35,36] and are also exhibited using short vertical lines at the bottom for easy comparison.

As mentioned above, the crystal structure of $TiSe_3$ has strong anisotropy. Thus, the electrical transport properties of $TiSe_3$ could be tuned by external pressure. Firstly, the electrical transport measurements of $TiSe_3$ were performed at ambient temperature and high pressure, as shown in Fig. 5(a). The resistivity initially increases and then decreases, changing by three orders of magnitude. For TiS_3, an isostructural TMT of $TiSe_3$, recent experimental and theoretical studies reported that the semiconducting behavior could be enhanced with the application of pressure up to 12 GPa.[37] Upon further compression, a pressure-induced semiconductor-to-metal transition occurs above 22 GPa. Theoretical calculations even predicted possible superconductivity with a transition temperature T_C of 9.3 K at 80 GPa.[38] These results inspired us to perform high-pressure transport study on $TiSe_3$.

The high-pressure and low-temperature electrical transport measurements on $TiSe_3$ were carried out using CAC equipment, as shown in Fig. 5(b). $TiSe_3$ shows semiconducting behavior at pressures lower than 2 GPa, and then exhibits a metallic state as the pressure further increases above 4 GPa. It is unlikely to be caused by the band-gap closing mechanism because it usually induces gradual conduction change, rather than an abrupt semiconductor-to-metal transition without any intermediate state as observed herein. This suggests that the transition mechanism might involve other effects such as the orbital variations of Se, which should be further investigated in future. The pressure at which the semiconductor-to-metal transition occurs ($\sim$4 GPa) in $TiSe_3$ is significantly lower than that in TiS_3 (22 GPa).[37] Unfortunately, pressure-induced superconductivity was not observed in $TiSe_3$ up to 13 GPa and 1.6 K.

Figures 5(c) and 5(d) show the temperature dependence of resistivity and its first-order derivative under 4 GPa and 5 GPa, respectively. Notably, there is a remarkable variation in $d\rho(T)/dT$ versus T, indicating the occurrence of a pressure-induced phase transition in $TiSe_3$. The phase transition temperatures are $T^* = 296$ K at 4 GPa and $T^* = 288$ K at 5 GPa, as estimated by extrapolating the linear fit of the $d\rho(T)/dT$ data. The mechanism of this pressure-induced phase transition is currently unknown and should be investigated in the future. Furthermore, a kink in the $\rho(T)$ curve, marked with arrows in Fig. 5(e), suggests a pressure-induced phase transition in $TiSe_3$. To further explore this mechanism, the magnetic field dependence of $\rho(T)$ was measured. Figure 5(f) shows that the kink in the $\rho(T)$ curve does not shift under 0.2 T compared to 0 T.

Figures 6(a)–6(h) depict the temperature dependence of resistivity and its first-order derivative under high pressure from 5.5 GPa to 13 GPa. A kink marked by blue dashed lines in the $\rho(T)$ curves under high pressure between 5.5 GPa and 10 GPa is visible, likely indicating the appearance of a certain phase transition which could be caused by magnetic ordering, CDW or Lifshitz transition.[39] First of all, the magnetic order in $TiSe_3$ can be ruled out due to its nonmagnetic nature. The I–V curve measured under 6.5 GPa and 2 K is shown as the inset of Fig. 6(i), which displays no saturation voltage or regular fluctuation related to CDW, as seen from the differential resistance (dV/dI). Besides, the voltage changes linearly with increasing current at 2 K, indicating that $TiSe_3$ is a pure metal likely without a CDW state under 6.5 GPa, [40,41] which is further supported by the theoretical calculations presented later. Instead, the kink in the $\rho(T)$ curve for $TiSe_3$ under high pressure is proposed to resulted from a Lifshitz transition. The pressure dependence of the Lifshitz transition temperature (T_L)

is plotted in Fig. 6(i), where T_L shows a dome-shaped variation with pressure, peaking at $T_L = 130.4$ K under 8 GPa.

Figure 7(a) presents the selected HP-XRD patterns of $TiSe_3$ under various pressures, which show that all diffraction peaks shift to higher diffraction angles as pressure increases. No splitting or appearance of new diffraction peaks below 14.5 GPa is visible. The result indicates that there is no pressure-induced structural phase transition in $TiSe_3$ within this pressure range. Therefore, the lattice parameters refinement and peak fitting of $TiSe_3$ are based on the space group $P2_1/m$. Figures 7(b) and 7(c) show the results of typical Rietveld refinements on $TiSe_3$ in the $P2_1/m$ phase under 1.6 GPa and 14.5 GPa, respectively, confirming the structural stability of $TiSe_3$ up to 14.5 GPa.

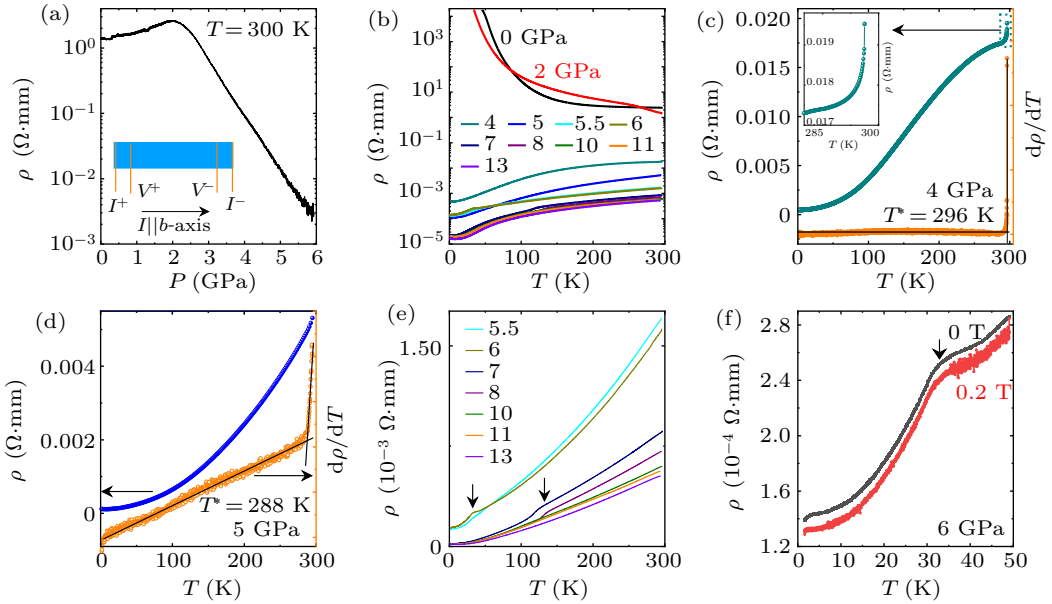


Fig. 5. (a) Pressure dependence of resistivity for $TiSe_3$ under ambient temperature. The inset shows the schematic measurement configuration. (b) Temperature dependence of resistivity as the pressure increases from 0 GPa to 13 GPa, where a remarkable pressure-induced semiconductor-to-metal transition is observed. (c) and (d) Temperature dependence of resistivity and its first-order derivative under 4 GPa and 5 GPa, where an unknown phase transition was marked with an asterisk. (e) Resistivity as a function of temperature under selected pressures (5.5 GPa to 13 GPa), where the appearance of kinks in $\rho(T)$ curves is labeled with arrows. (f) Lower temperature part of $\rho(T)$ at 6 GPa under a magnetic field.

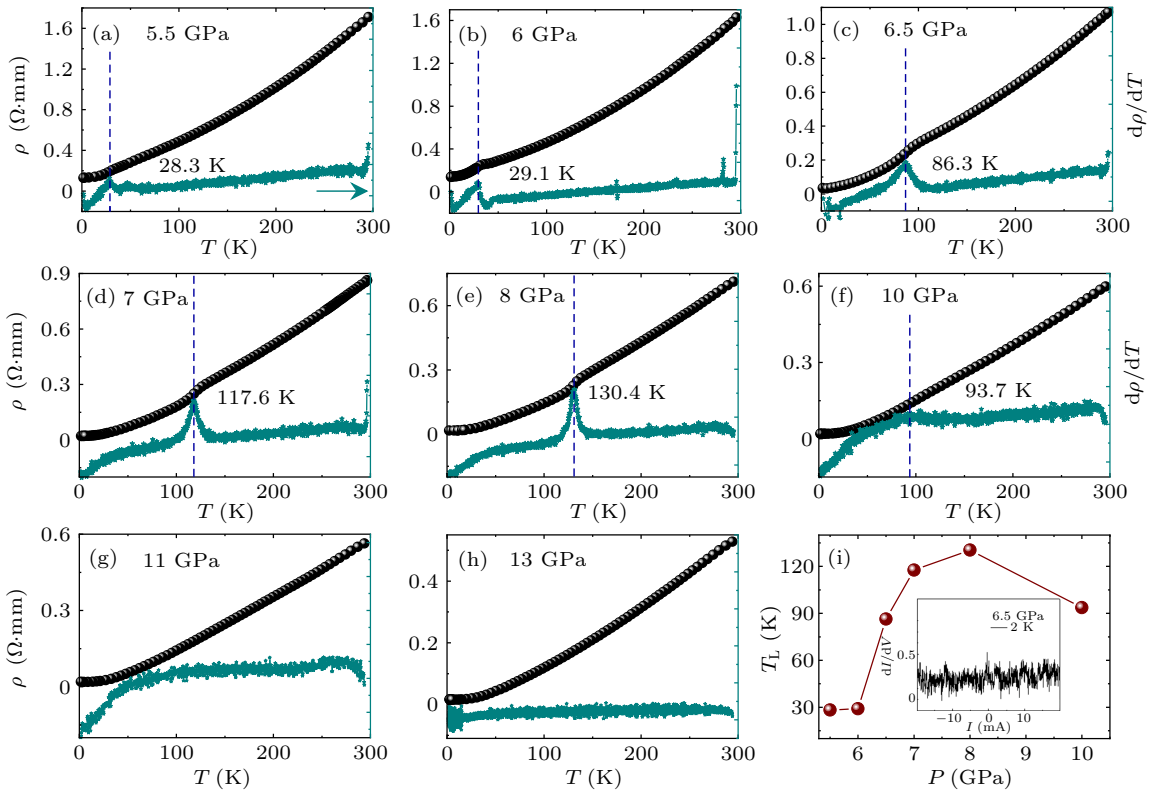


Fig. 6. (a)–(h) Temperature dependence of resistivity and the the first-order derivative under high pressure between 5.5 GPa and 13 GPa. The Lifshitz transition is marked with blue dashed lines. (i) Lifshitz transition temperature as a function of pressure; the inset shows the differential resistance (dV/dI) at 6.5 GPa and 2 K.

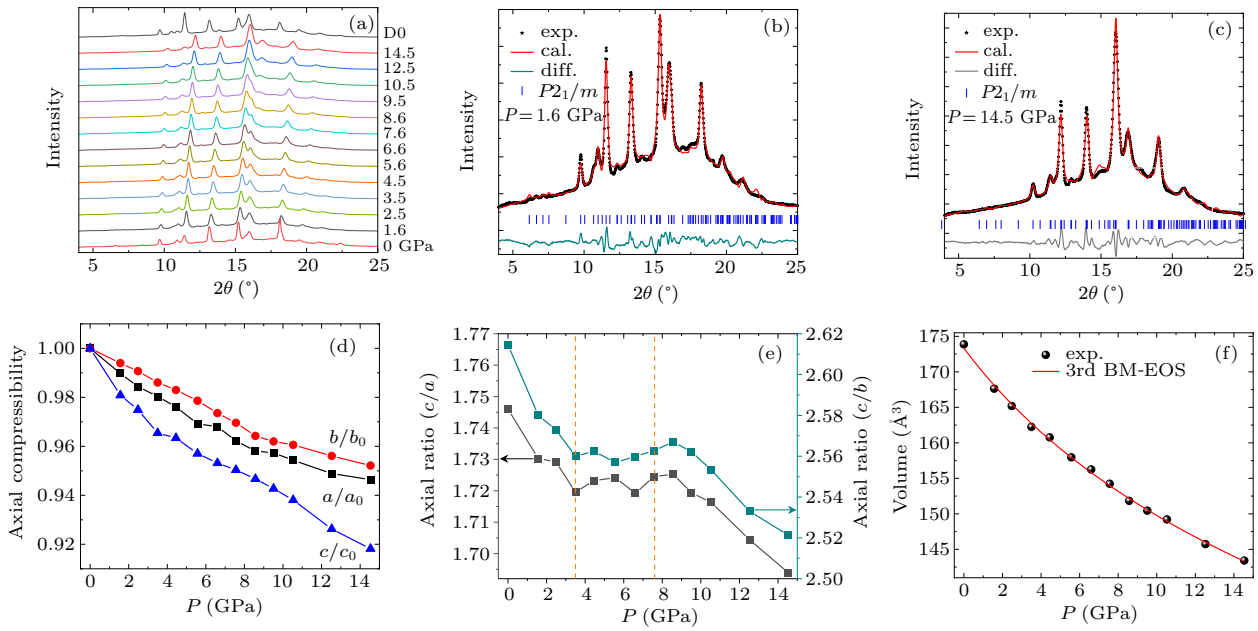


Fig. 7. (a) HP-XRD patterns of $TiSe_3$ under various pressures up to 14.5 GPa at room temperature. The XRD pattern collected upon pressure release to ambient conditions is marked as D0. (b) and (c) Results of typical Rietveld structural refinement of $TiSe_3$. The vertical bars represent the calculated positions of the diffraction peaks for $P2_1/m$ phase of $TiSe_3$. The difference between the experimental (exp.) and the calculated (cal.) patterns is shown as a gray line at the bottom of the diffraction peaks. (d) Pressure dependence of axial compressibility a/a_0, b/b_0, and c/c_0. (e) Axial ratios c/a and c/b as functions of pressure. (f) Pressure dependence of volume for $TiSe_3$ and the fitting using the 3rd-order BM-EOS.

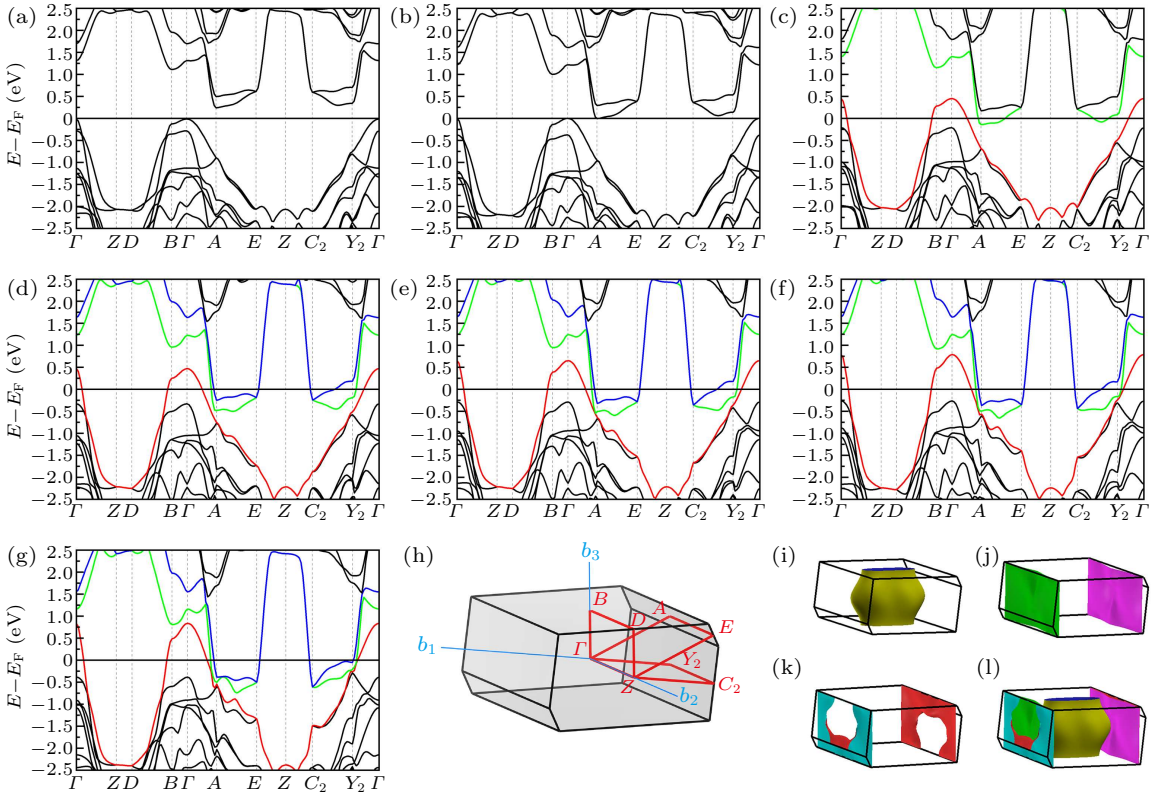


Fig. 8. Band structures calculated with the hybrid functional HSE06 at (a) ambient pressure, (b) 1 GPa, (c) 2 GPa, (d) 4 GPa, (e) 6 GPa, (f) 8 GPa, and (g) 10 GPa, respectively. (h) The first Brillouin zone and the high-symmetry k-path adopted for band structure calculations. (i)–(k) Fermi surfaces at 8 GPa corresponding to the bands indicated by the red, green, and blue lines, respectively. (l) The merged Fermi surface at 8 GPa.

Figure 7(d) shows the axial compressibility of $TiSe_3$, i.e., a/a_0, b/b_0, and c/c_0, as a function of pressure, revealing that the c-axis is more compressible than those of the a- and b-axes. The anisotropic compressibility of $TiSe_3$ is due to the weak vdW coupling along the c-axis and the quasi-1D chains along the b-axis. A Lifshitz phase transition in the R-3m phase of Bi_2Te_3 and Bi_2Se_3 leads to a pronounced c/a ratio change at $\sim$ 3 GPa.[42,43] The axial ratios, c/a and c/b of $TiSe_3$, show a saddle-shape variation between $\sim$ 4–8 GPa, as shown in Fig. 7(e), thus supporting crystallographic evidence

for a pressure-induced Lifshitz phase transition in $TiSe_3$. The pressure-induced Lifshitz phase transition with a concomitant axial ratio variation was also found in other quantum materials such as ZrSiTe[44] and BiTeBr.[45]

At last, the pressure-volume data of $TiSe_3$ were fitted by using the third-order Birch–Murnaghan equation of state (BM-EOS)[46]

$$P(V) = \frac{3}{2} \times B_0 \times \left[\left(\frac{V_0}{V} \right)^{7/3} - \left(\frac{V_0}{V} \right)^{5/3} \right] \times \left\{ 1 + \frac{3}{4} \times (B_0' - 4) \times \left[\left(\frac{V_0}{V} \right)^{2/3} - 1 \right] \right\},$$

where B_0 is the bulk modulus, V_0 is the lattice volume at ambient pressure, and B_0' is the first-order derivative of B_0. The experimental and fitting results are presented in Fig. 7(f), yielding a bulk modulus of $B_0 = 47.4(1)$ GPa, $V_0 = 173.3(3)$ Å^3, and $B_0' = 5.0(1)$. The small bulk modulus of 47.4(1) GPa is due to the quasi-1D crystalline and vdW force characteristic of $TiSe_3$.

The band structures and Fermi surface of $TiSe_3$ at selected pressures, as shown in Fig. 8, were calculated using the Heyd–Scuseria–Ernzehof functional. It shows semiconducting behavior with a narrow indirect gap of approximately 0.26 eV from Γ to A at ambient pressure, which is consistent with experimental observations. When the pressure reaches 1 GPa, the conduction band minimum and the valence band maximum touch the Fermi level at A and Γ points in the reciprocal space, respectively, indicating a typical semimetallic characteristic.

As the pressure increases, two bands crossing the Fermi level appear at 2 GPa. The band in red forms an elliptical cylindrical hole sheet around Γ point, and the band in green forms two rectangular electron sheets along the A–E and C_2–Y_2 paths. The theoretically simulated semiconductor-to-metal transition coincides well with that observed in the transport measurements. From 2 GPa to 4 GPa, one additional band marked by blue crosses the Fermi level, forming two rectangular electron sheets with a hollow in the center along the A–E and C_2–Y_2 paths. The result supports the pressure-induced Lifshitz transition, as also suggested by the kink variation in the $\rho(T)$ curve and the discontinuity in the pressure dependence of the axial ratio c/a. Up to 10 GPa, the electron sheets contributed by the green and blue bands become slightly larger and the hole sheet remains almost unchanged compared with 4 GPa.

4. Conclusion and perspectives

We successfully synthesized a new quasi-1D material $TiSe_3$ and grew the single crystals by using the HPHT technique. The crystal structures under ambient pressure and high pressure up to 14.5 GPa at room temperature were investigated. Our electrical and magneto-transport measurements revealed that $TiSe_3$ is a narrow band gap semiconductor at ambient pressure, while it exhibits a pressure-induced semiconductor-to-metal transition at ~ 4 GPa. The kink in the $\rho(T)$ curve was ascribed to a Lifshitz transition as the pressure increases to 6 GPa. Because $TiSe_3$ is a layered material with weak interlayer van der Waals coupling, it is therefore easily exfoliated into different layers. This virtue makes it a promising material for future use in devices.

Acknowledgements

The authors acknowledge the National Key R&D Program of China (Grant Nos. 2023YFA1406100 and 2024YFA1400066). Y. Guo acknowledges the Open Research Fund of Beijing National Laboratory for Condensed Matter Physics (Grant No. 2023BNLCMPKF002). L. Wang was mainly supported by the National Natural Science Foundation of China (Grant Nos. 52288102 and 52090020) and the S&T Program of Hebei (Grant No. 225A1102D). Z. Yu acknowledges the Open Projects from the State Key Laboratory of Metastable Materials Science and Technology, Yanshan University (Grant No. 202301). A portion of this work was carried out at the Synergetic Extreme Condition User Facility (SECUF) of the Chinese Academy of Sciences. The authors also thank the support from the Analytical Instrumentation Center (Grant No. SPST-AIC10112914), School of Physical Science and Technology (SPST), ShanghaiTech University. This project was also supported by the Double First-Class Initiative Fund of ShanghaiTech University.

References

[1] Novoselov K S, Geim A K, Morozov S V, Jiang D, Zhang Y, Dubonos S V, Grigorieva I V and Firsov A A 2004 *Science* **306** 666
[2] Koppens F H L, Mueller T, Avouris Ph, Ferrari A C, Vitiello M S and Polini M 2014 *Nat. Nanotechnol.* **9** 780
[3] Manzeli S, Ovchinnikov D, Pasquier D, Yazyev O V and Kis A 2017 *Nat. Rev. Mater.* **2** 17033
[4] Xu X D, Yao W, Xiao D and Heinz T F 2014 *Nat. Phys.* **10** 343
[5] Mak K F and Shan J 2016 *Nat. Photonics* **10** 216
[6] Island J O, Molina-Mendoza A J, Barawi M, Biele R, Flores E, Clamagirand J M, Ares J R, Sánchez C, van der Zant H S J, Agosta R D, Ferrer I J and Castellanos-Gomez A 2017 *2D Mater.* **4** 022003
[7] Chen M D, Li L, Xu M Z, Li W W, Zheng L and Wang X W 2023 *Research* **6** 0066
[8] Grønvold F, Langmyhr F J and Stjernström N E 1961 *Acta Chem. Scand.* **15** 1949
[9] Hirota T, Ueda Y and Kosuge K 1988 *Mater. Res. Bull.* **23** 1641
[10] Abdulsalam M and Joubert D P 2015 *Eur. Phys. J. B* **88** 177
[11] Yang M X, Cao B H, Chen J J, Liang M, Sun Y M, Duan D F and Tian F B 2023 *Phys. Lett. A* **491** 129209
[12] Merrill L 1977 *J. Phys. Chem. Ref. Data* **6** 1205
[13] Merrill L 1982 *J. Phys. Chem. Ref. Data* **11** 1005
[14] Liu X L, Yu Z H, Liang Q F, Zhou C Y, Wang H Y, Zhao J G, Wang X, Yu N, Zou Z Q and Guo Y F 2020 *Chem. Mater.* **32** 8781
[15] Dolomanov O V, Bourhis L J, Gildea R J, Howard J A K and Puschmann H 2009 *J. Appl. Crystallogr.* **42** 339

[16] Sheldrick G M 2015 *Acta Crystallogr. A* **71** 3
[17] Sheldrick G M 2015 *Acta Crystallogr. C* **71** 3
[18] Mao H K, Xu J and Bell P M 1986 *J. Geophys. Res.* **91** 4673
[19] Larson A C and Von Dreele R B 2000 *General Structure Analysis System (GSAS)*, Los Alamos National Laboratory Report LAUR 86-748
[20] Toby B H 2001 *J. Appl. Cryst.* **34** 210
[21] Thomasson J, Ayache C, Spain I L and Villedieu M 1990 *J. Appl. Phys.* **68** 5933
[22] Hohenberg P and Kohn W 1964 *Phys. Rev*. **136** B864
[23] Kohn W and Sham L J 1965 *Phys. Rev*. **140** A1133
[24] Blochl P E 1994 *Phys. Rev. B* **50** 17953
[25] Kresse G and Joubert D 1999 *Phys. Rev. B* **59** 1758
[26] Kresse G and Furthmüller J 1996 *Phys. Rev. B* **54** 11169
[27] Kresse G and Furthmüller J 1996 *Comput. Mater. Sci.* **6** 15
[28] Grimme S, Antony J, Ehrlich S and Krieg S 2010 *J. Chem. Phys.* **132** 154104
[29] Krukau A V, Vydrov O A, Izmaylov A F and Scuseria G E 2006 *J. Chem. Phys.* **125** 224106
[30] Jellinek F, Pollak R A and Shafer M W 1974 *Mater. Res. Bull.* **9** 845
[31] Jin Y D, Li X X and Yang J L 2015 *Phys. Chem. Chem. Phys* **17** 18665
[32] Saeed Y, Kachmar A and Carignano M A 2017 *J. Phys. Chem. C* **121** 1399
[33] Bremholm M, Hor Y S and Cava R J 2011 *Solid State Sci.* **13** 38
[34] Srivastava S K and Avasthi B N 1992 *J. Mater. Sci.* **27** 3693
[35] Osada K, Bae S, Tanaka M, Raebiger H, Shudo K and Suzuki T 2016 *J. Phys. Chem. C* **120** 4653
[36] Khatibi A, Godiksen R H, Basuvalingam S B, Pellegrino D, Bol A A, Shokri B and Curto A G 2019 *2D Mater.* **7** 015022
[37] An C, Lu P C, Chen X L, Zhou Y H, Wu J F, Zhou Y, Park C, Gu C C, Zhang B W, Yuan Y F, Sun J and Yang Z R 2017 *Phys. Rev. B* **96** 134110
[38] Zhong X, Zhang M, Yang L, Qu X, Yang L, Yang J and Liu H 2019 *Comput. Mater. Sci.* **158** 192
[39] Li Z X, Chen X J, Liu X L, Yu Z H, Su N, Liu Z Y, Xia W, Jiao J L, Zhou C Y, Zhang L L, Dong Z H, Wang X, Yu N, Zou Z Q, Ma J, Cheng J G, Zhong Z C and Guo Y F 2023 *J. Alloys Compd.* **937** 168337
[40] Sinchenko A A, Lejay P, Leynaud O and Monceau P 2016 *Phys. Rev. B* **93** 235141
[41] Yao M L, Liu W S, Chen X, Ren Z S, Wilson S, Ren Z F and Opeil C P 2017 *J. Materiomics* **3** 150
[42] Polian A, Gauthier M, Souza S M, Trichês D M, Cardoso De Lima J and Grandi T A 2011 *Phys. Rev. B* **83** 113106
[43] Yu Z H, Wang L, Hu Q Y, Zhao J G, Yan S, Yang K, Sinogeikin S, Gu G and Mao H 2015 *Sci. Rep.* **5** 15939
[44] Krottenmüller M, Vöst M, Unglert N, Ebad-Allah J, Eickerling G, Volkmer D, Hu J, Zhu Y L, Mao Z Q, Scherer W and Kuntscher C A 2020 *Phys. Rev. B* **101** 081108(R)
[45] Ohmura A, Higuchi Y, Ochiai T, Kanou M, Ishikawa F, Nakano S, Nakayama A, Yamada Y and Sasagawa T 2017 *Phys. Rev. B* **95** 125203
[46] Birch F 1947 *Phys. Rev.* **71** 809